Free-Standing Two-Dimensional Single-Crystalline InSb Nanosheets

D. Pan,[†] D. X. Fan,[‡] N. Kang,[‡] J. H. Zhi,[‡] X. Z. Yu,[†] H. Q. Xu,*,[‡] and J. H. Zhao*,[†]

[†]State Key Laboratory of Superlattices and Microstructures, Institute of Semiconductors, Chinese Academy of Sciences, P.O. Box 912, Beijing 100083, China

[‡]Key Laboratory for the Physics and Chemistry of Nanodevices and Department of Electronics, Peking University, Beijing 100871, China

Ⓢ Supporting Information

ABSTRACT: Growth of high-quality single-crystalline InSb layers remains challenging in material science. Such layered InSb materials are highly desired for searching for and manipulation of Majorana Fermions in solid state, a fundamental research task in physics today, and for development of novel high-speed nanoelectronic and infrared optoelectronic devices. Here, we report on a new route toward growth of single-crystalline, layered InSb materials. We demonstrate the successful growth of free-standing, two-dimensional InSb nanosheets on one-dimensional InAs nanowires by molecular-beam epitaxy. The grown InSb nanosheets are pure zinc-blende single crystals. The length and width of the InSb nanosheets are up to several micrometers and the thickness is down to ~10 nm. The InSb nanosheets show a clear ambipolar behavior and a high electron mobility. Our work will open up new technology routes toward the development of InSb-based devices for applications in nanoelectronics, optoelectronics, and quantum electronics and for the study of fundamental physical phenomena.

KEYWORDS: Free-standing layered InSb, single-crystalline, mobility, molecular-beam epitaxy
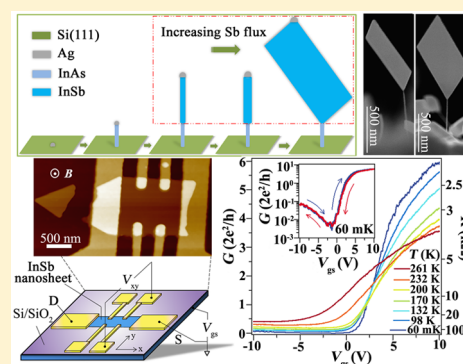
O ver the past several decades, the inherent scaling limitations of Si electron devices have fuelled the exploration of alternative semiconductors with high carrier mobility to further enhance device performance.[1−3] In particular, high mobility III−V compound semiconductors have been actively studied.[4,5] As a technologically important III−V semiconductor, InSb is the most desired material system for applications in high-speed, low-power electronics and infrared optoelectronics owing to its highest electron mobility and narrowest bandgap among all the III−V semiconductors. Recently, epitaxially grown InSb nanostructures have been widely anticipated to have potential applications in spintronics, topological quantum computing, and detection and manipulation of Majorana Fermions, due to small effective mass, strong spin−orbit interaction and giant g factor in InSb.[6−18] All these applications require a high degree of InSb growth control on its morphology and especially crystal quality.[19,20] Unfortunately, because of the intrinsic largest lattice parameter of InSb among all the III−V semiconductors, epitaxial growth of InSb layers faces an inevitable difficulty in finding a lattice-matched substrate. Conventionally, buffer layers with graded or abrupt composition profile are deposited on lattice mismatched substrates to obtain a layer with a required value of lattice constant.[21,22] Nevertheless, even when the sophisticated buffer-layer engineering is used, the density of dislocations threading to the surface of the buffer from its interface with a lattice mismatched substrate is often too high to grow a high crystal quality InSb layer for fabrication of high-performance nano-

electronics and quantum devices and for study of novel physical phenomena.

In this Letter, we report on the successful growth of novel free-standing high-quality two-dimensional (2D) InSb nanosheets by molecular-beam epitaxy (MBE). A new route of growing high material quality layered InSb structures is discovered in which free-standing InSb nanosheets are epitaxially grown on InAs nanowire stems and thus the process is independent of buffer-layer engineering. The morphology and size of free-standing InSb nanosheets can be controlled in the approach by tailoring the Sb/In beam equivalent pressure (BEP) ratio and InSb growth time. We demonstrate the growth of free-standing InSb nanosheets with the length and width up to several micrometers and the thickness down to ~10 nm. High-resolution transmission electron microscope (TEM) images show that the grown InSb nanosheets are pure zinc-blende (ZB) single crystals and have excellent epitaxial relationships with the InAs nanowire stems. The formation of the InSb nanosheets is attributed to a combination of vapor−liquid−solid (VLS) and lateral growth. Electrical measurements show that the grown InSb nanosheets exhibit an ambipolar behavior and a high electron mobility. These novel, high material quality, free-standing InSb single-crystalline nano-
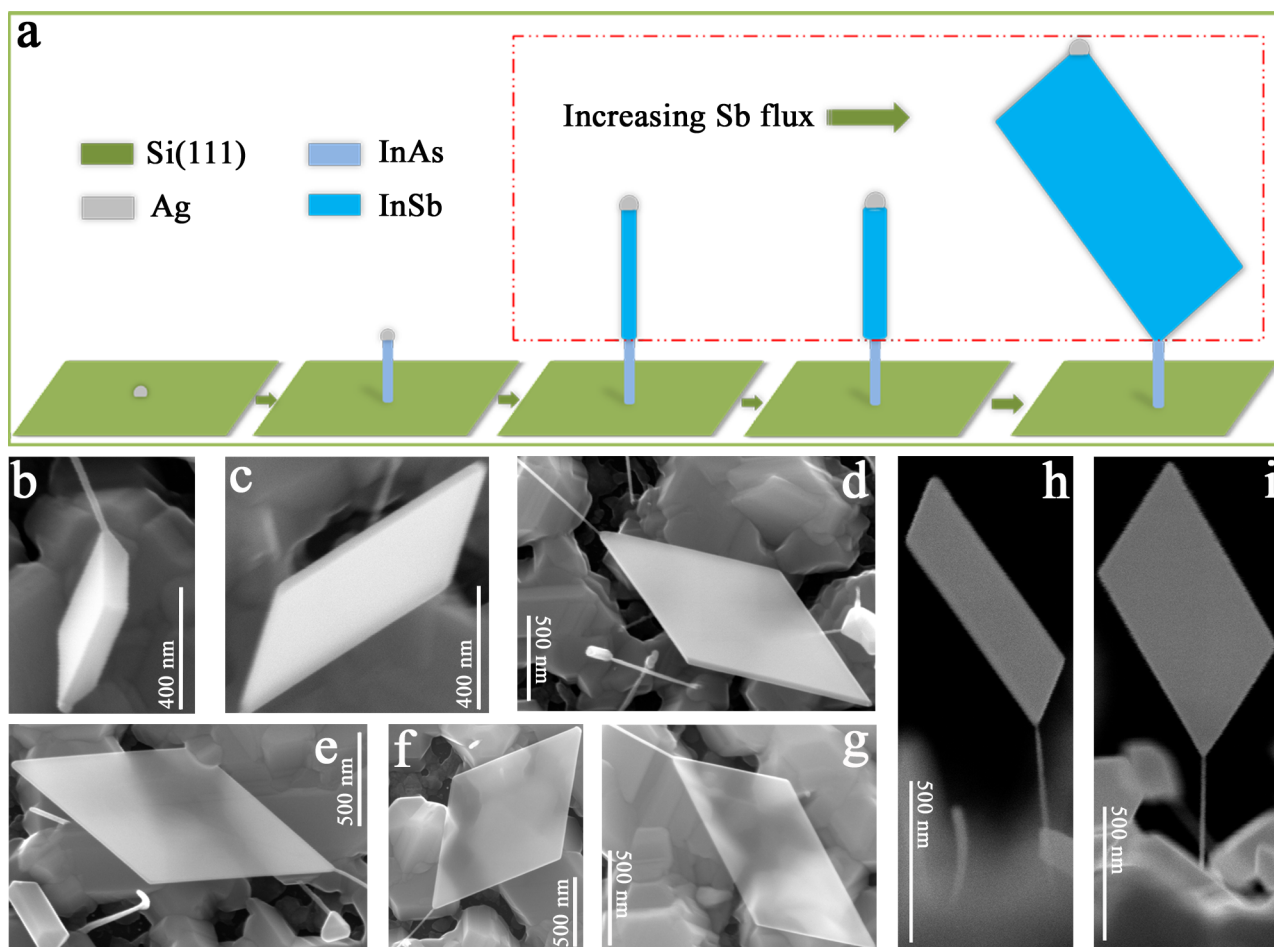
Figure 1. Diagram of the growth process and SEM images of the InSb nanosheets. (a) Schematic demonstration of the growth process of the 2D InSb nanosheets. By tailoring the Sb/In BEP ratio, the 2D InSb nanosheets were epitaxially grown on free-standing InAs nanowire stems that were first grown on Si(111) substrates using Ag as catalyst. (b−g) and (h−i) Top and side view SEM images of the InSb nanosheet epitaxially grown on 1D InAs nanowires with an Sb/In BEP ratio of 80, respectively.

sheets have the great potential not only for applications in high-speed electronics and infrared optoelectronics but also for realization of novel quantum devices for the studies of fundamental physics.

All the InAs/InSb nanostructures were grown in a solid source MBE system (VG 80) equipped with standard Knudsen-cells. Commercial p-type Si (111) wafers were used as the substrates. Before loading the Si substrates into the MBE chamber, they were immersed in a diluted HF (2%) solution for 1 min to remove the surface contamination and native oxide. After cleaning, a Ag layer of 2 Å nominal thickness was deposited on the substrate in the MBE growth chamber at room temperature and then annealed in situ at 650 °C for 20 min to generate Ag nanoparticles. InAs nanowires were grown for 20 min at a temperature of 505 °C with an As/In BEP ratio of 30 (the beam fluxes of In and As_4 sources are 1.0×10^{-7} and 3.0×10^{-6} mbar, respectively).[23] Then the group-V source was abruptly switched from As to Sb without any variation of substrate temperature. All the InSb segments (if no specific description) were grown for 80 min at different Sb/In BEP ratios by increasing the Sb flux (ranging from 1.0×10^{-7} to 1.2×10^{-5} mbar) while keeping the In flux constant.

For device fabrication, the as-grown InSb nanosheets were first mechanically transferred to a degenerately n-doped Si substrate covered by 105 nm SiO_2 layer, which serves as a global back gate. Then selected nanosheets were optically positioned relative to predefined alignment marks. Finally, the contact electrodes were patterned onto the sample using standard electron-beam lithography process. Prior to electron-beam evaporating a layer of 10/100 nm Ti/Au metal film, the sample was chemically etched for 2 min in a DI water-diluted $(NH_4)_2S_x$ solution to remove the surface oxide layer at the contact area. All electrical measurements in this work were performed in a ^{3}He/^{4}He dilution fridge with a base temperature of 8 mK (Oxford Triton 200). In the two-probe measurements, only the source/drain (S/D) contacts were dc voltage-biased, and the other four contacts were left floated. In the Hall-bar measurements, the S/D contacts were used to inject a constant dc current bias of ∼50 nA through the sample, and the Hall voltage V_{xy} was amplified and recorded simultaneously with respect to the sweep of the magnetic field applied perpendicularly to the plane of the sample/substrate. In the two-probe $G−V_{gs}$ data, a circuit resistance of ∼21.56 kΩ (including RC filters and series resistors) has been subtracted.

The 2D InSb nanosheets were grown on free-standing InAs nanowire stems that were first grown on Si(111) substrates using Ag as catalyst in the MBE chamber. Figure 1a shows the schematics for the growth process. We found that the morphology of InSb strongly depends on the Sb/In BEP ratio, and the InSb nanosheets can be realized by tailoring the
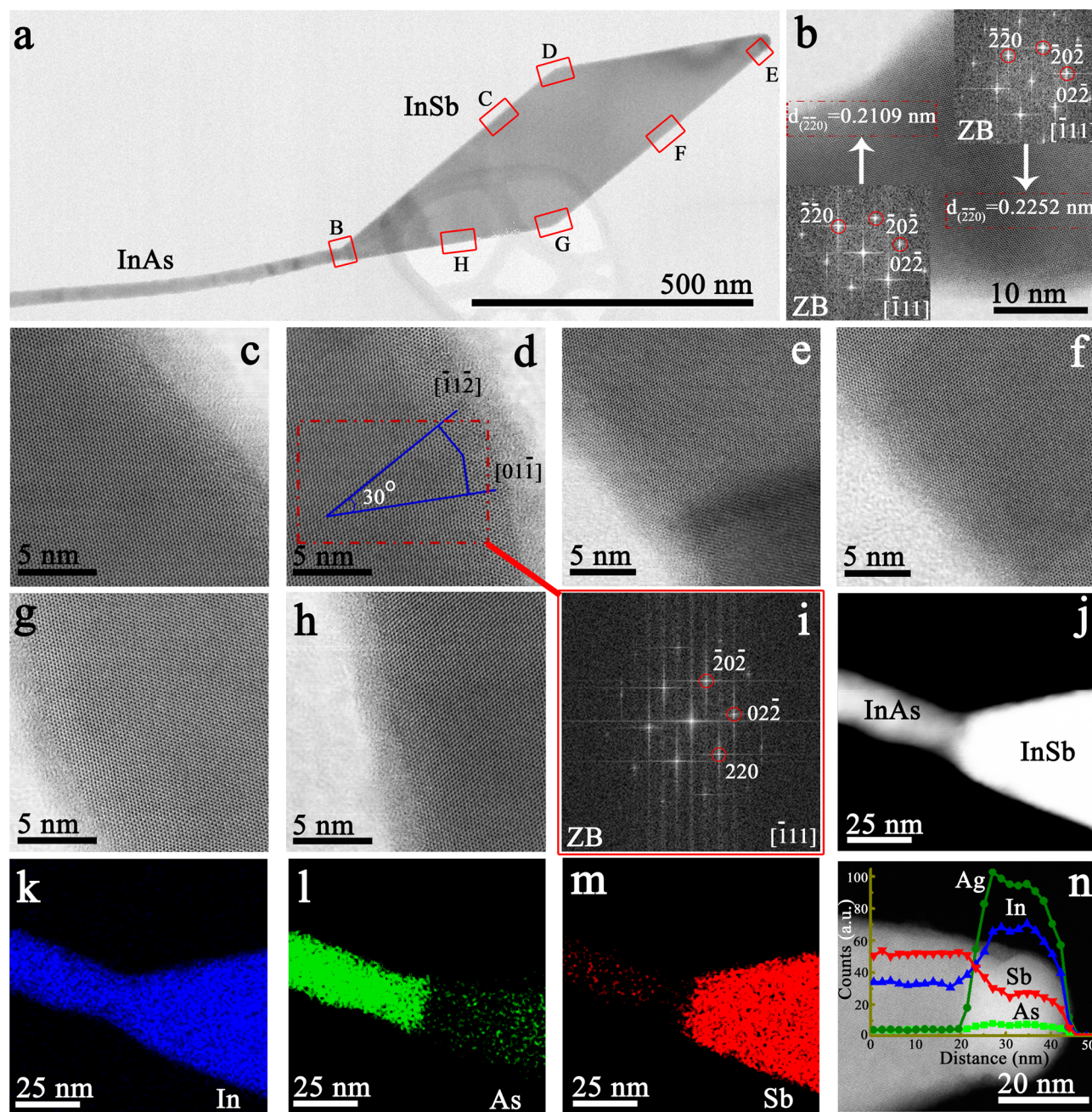
Figure 2. Crystal structure and chemical composition of an InSb nanosheet. (a) Low-resolution TEM image of an InAs/InSb nanowire-nanosheet grown with an Sb/In BEP ratio of 27. The red rectangles highlight the regions where the high-resolution TEM images were recorded. (b) High-resolution TEM image taken from the InAs/InSb interface (region B in (a)). The left and right insets are the corresponding FFTs of the InAs and InSb segments, respectively. The interplanar spacings of the InAs and InSb segments were measured using a standard digital micrograph software. (c−h) High-resolution TEM images taken from the regions C, D, E, F, G, and H in (a), respectively. (i) FFT pattern corresponding to (d). (j,k−m) HAADF-STEM image of the InAs/InSb interface area and false-color STEM EDS elemental maps of In, As, and Sb in the region of the InAs/InSb junction, respectively. (n) HAADF-STEM image of the InSb nanosheet in the region covering the InSb/seed-particle interface with overlaid EDS profiles.

Sb/In BEP ratio (see Supporting Information Section S1). For the sample grown with low Sb/In BEP ratio of 1−20, InSb and InAs formed core−shell or axial heterostructure nanowires (see Supporting Information Figures S1 and S2). Further increasing the Sb/In BEP ratio, the resulting InSb nanowires have diameters obviously larger than that of the InAs segment (detailed TEM investigation of a dozen of such nanowires reveals a diameter increase from 130 to 589%, see Supporting Information Figure S3 and Table S1). By increasing the Sb/In

BEP ratio to the range of 27−80, new geometrically structured materials with each consisting of a 2D InSb nanosheet and a 1D InAs nanowire stem were obtained (see Supporting Information Figures S1 and S4−S6). Figure 1b−g shows the top-view magnified scanning electron microscope (SEM) images of InSb nanosheets grown with an Sb/In BEP ratio of 80. As can be seen, the grown InSb nanosheets have parallelogram shapes. The thicknesses of the InSb nanosheets show significant variation (see Supporting Information Figure S7), as measured
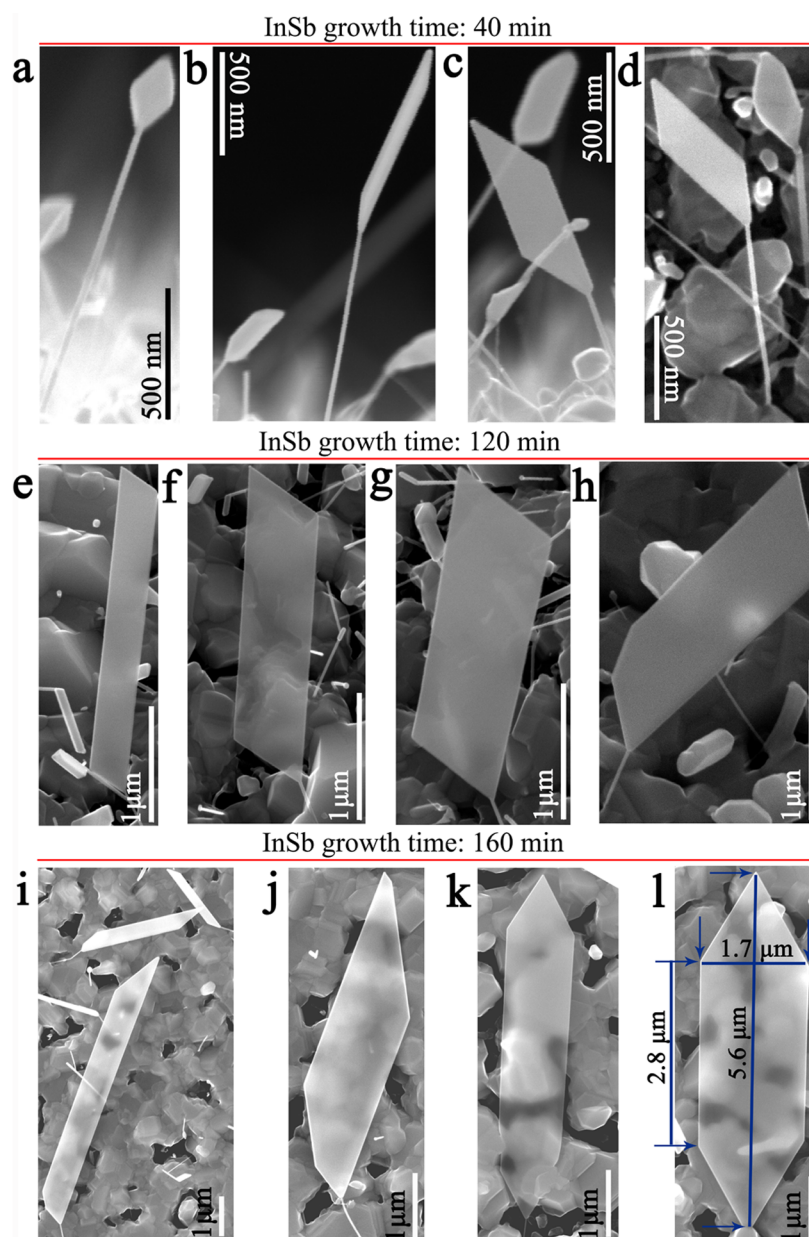
Figure 3. Size controlling of the InSb nanosheets by tailoring the InSb growth time. (a−c,d) Side and top view SEM images of the InSb nanosheets with the growth time of 40 min, respectively. (e−g,h) The 20° tilted and top view SEM images of the InSb nanosheets with the growth time of 120 min, respectively. (i−l) Top view SEM images of the InSb nanosheets with the growth time of 160 min.

from SEM images, from ∼67 nm (Figure 1b), to ∼30 nm (Figure 1c,d), and to the ultrathin value of ∼10 nm (Figure 1e,g). The ultrathin nanosheets can be penetrated easily by the electron beam of the SEM. (In Figure 1e−g, features on the substrate surface are clearly visible through the thin InSb nanosheets.) Figure 1h,i shows the side-view magnified SEM images of InSb nanosheets in the same sample and it is clear that the InSb nanosheets can be grown on ultrathin InAs nanowires (∼10 nm in diameter) that are oriented perpendicular to the substrate surface with a pure wurtzite (WZ) crystal structure.[23]

To examine the structural characteristics, crystalline quality, and the chemical composition of the grown InSb nanosheets, TEM and energy dispersive X-ray spectroscopy (EDS) measurements were performed. Figure 2a is a bright-field TEM image of a typical InSb nanosheet grown on an InAs

nanowire at an Sb/In BEP ratio of 27. The InAs stem is 21 nm in diameter and 725 nm in length, while the InSb segment has a parallelogram shape with side lengths of 380 and 508 nm. It is found that the 2D InSb nanosheets can be successfully grown not only on 1D WZ crystalline InAs nanowires (see Supporting Information Figure S8) but also on 1D InAs nanowires with ZB phase, as shown in Figure 2b. High-resolution TEM images of the side sections (Figure 2c,f,h), the corner sections (Figure 2d,g) and the section near the tip (Figure 2e) of the InSb nanosheet and the associated Fourier transform (Figure 2i) illustrate that the InSb nanosheet has a perfect ZB crystal structure, free from stacking faults or WZ regions. Although the stacking faults have been observed in Ag-catalyzed and self-seeded InSb nanowires by other groups,[24,25] detailed TEM observations of our grown InSb nanosheets with different shapes and sizes all reveal that the InSb nanosheets are fully
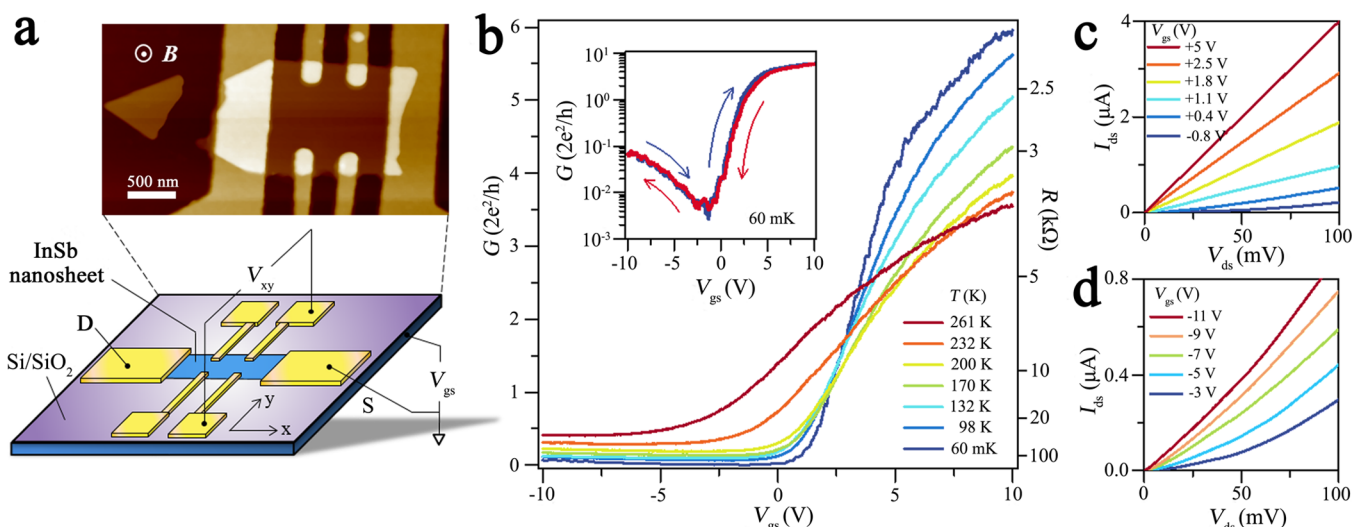
Figure 4. Transport properties of the InSb nanosheets. (a) Schematic diagram (lower panel) and atomic force microscopy image (upper panel) of typical InSb nanosheet Hall-bar device. A voltage bias is applied to the S and D electrode in a two-probe measurement setup, while a current bias is applied to the S and D electrode in the Hall measurement setup. A global back gate voltage V_{gs} is applied to the degenerately doped Si substrate. The magnetic field is perpendicular to the plane of the sample. (b) Two-probe conductance G as a function of V_{gs} at different temperatures (Device 1). Here, the nanosheet thickness of Device 1 is 50 nm. In the measurements, the S−D bias V_{ds} applied is between 10 mV (near pinch-off) and ∼1 mV (at V_{gs} = 10 V). Note that the right axis shows the two-probe resistance $R = 1/G$. The inset shows a logarithmic scale plot of the $G−V_{gs}$ curve at T = 60 mK. Both the upward (blue) and downward (red) sweep show a clear ambipolar characteristic and a small hysteresis (of ∼0.8 V). (c) Corresponding current−voltage characteristics at different back gate voltages in the electron transport region. (d) Corresponding current−voltage characteristics at different back gate voltages in the hole transport region.

single-crystalline, completely free from stacking faults and twinning defects (see Supporting Information Figures S9 and S10). As observed in InSb nanocrystals grown with a high Sb/In BEP ratio,[26] the side facets with low surface energy such as {$\bar{1}$11} and {011} can be clearly seen in our InSb nanosheets (Figure 2d and Supporting Information Figure S9). High-angle annular dark-field scanning TEM (HAADF-STEM) and corresponding EDS line profiles (see Supporting Information Figure S11) show that the InAs/InSb heterostructures start as InAs and then change to InSb. EDS elemental mappings shown in Figure 2k−m confirm that clear interfaces formed between the InAs nanowires and the InSb nanosheets as reported in InAs/InSb heterostructure nanowires.[27−31] The remaining spherical catalyst particle on the top of InSb nanosheets is found to be composed of Ag, In, and Sb (Figure 2n). EDS point analysis of the InSb nanosheet gives an average atomic ratio of In/Sb = 50.9:49.1 (see Supporting Information Table S2). The contents of Ag, In, and Sb in the seed particles after the growth of the InSb nanosheets and of the InSb nanowires are similar (the measured average composition is Ag/In/Sb = 62.0:25.6:12.3, Ag/In/Sb = 63.2:25.2:11.4 for the seed particles of the InSb nanosheets and of the InSb nanowires, respectively; see Supporting Information Table S2).

The length and width of the InSb nanosheets can be controlled directly by tailoring the InSb growth time. Figure 3a−d shows the SEM images of the InSb nanosheets obtained with the InSb growth time of 40 min. Comparing to the InSb nanosheets obtained with the InSb growth time of 80 min (Figure 1 and Supporting Information Figure S1), no apparent difference in morphology is observed in these InSb nanosheets except for their smaller sizes. With increasing the InSb growth time to 120 min and to 160 min (Figure 3e−l and Supporting Information Figure S6) while keeping other growth parameters unchanged, the obtained InSb nanosheets are still in planar

shapes; these InSb nanosheets can be grown to micrometers in length and width, while still be kept in a thin thickness.

As to the growth mechanism of the InSb nanosheets, it is unlikely that the growth is governed solely by the traditional VLS or vapor−solid (VS) process.[32−34] On the contrary, we consider that the growth of the InSb nanosheets is dominated by the combination of VLS (vertical growth) and VS (lateral growth) processes. The spherical Ag−In−Sb alloy particles on the top of InSb nanowires and InSb nanosheets have the same crystal structure and the similar compositions (see Supporting Information Figure S12 and Table S2 and Figure 2n), indicating that the VLS mechanism for Ag-seed InSb nanowire growth[24] exists in the growth of the InSb nanosheets. Meanwhile, we find that the lateral growth observed often in the growth of antimonide nanowires[27−30,35−37] is incorporated into our InSb nonsheet growth, because the width of the nanosheets is growth time dependent (Figures 3a to 3l). On the basis of our observations, the InSb evolves from thin nanowires to thick nanowires and to nanosheets with only increasing Sb flux, indicating that the Sb flux is one of the key factors for InSb nanosheets growth. According to the literatures,[38,39] the growth rates of semiconductor nanowires can be changed by Sb addition due to its surfactant behavior. In our case, the axial and lateral growth rates of the InSb could also be changed with increasing the Sb flux and the morphological transformation of the InSb could be attributed to a competition and combination of the axial and lateral growth of the InSb. That is to say, for a low Sb flux used (e.g., Sb/In BEP ratio of 10, see Supporting Information Figure S1b), the InSb has a high axial growth rate (the lateral growth rate is low) and InSb nanowires with thin diameters can be obtained. With increasing the Sb flux (e.g., Sb/In BEP ratio larger than 27, see Supporting Information Figure S1c−e), the lateral growth becomes comparable to the axial growth or dominates the InSb growth, and the InSb nanosheets are obtained. Lin et al.[26] also found that InSb

morphologies can be changed from nanowires to pancake-like nanostructures by increasing the Sb flux and their calculations indicated that surface energy plays an important role in determining the shape of the InSb nanocrystal. The calculations on surface energies for the InSb nanosheet crystal facets are also important for us to understand the cubic InSb adopting a nanosheet structure, which will be explored in the next stage of our work. Very recently, Mata et al.[40] reported a twin-induced 2D-like crystal growth mode, which can be used to well explain the growth process of InSb nanosails grown on InP/InAs nanowire sterms. However, in this work detailed TEM results showed that our InSb nanosheets have pure ZB crystal structure, completely free from stacking faults and twinning defects. For the VLS and lateral growth processes of our InSb nanosheets, one possible model is given in Supporting Information Section S6. Although the exact growth process of the InSb nanosheets remains to be determined, we believe that the mechanism of combination of the VLS and the lateral growth could be used to fabricate other high-quality 2D antimonide nanostructures.

Electronic properties of the grown InSb nanosheets were characterized by electrical measurements. Figure 4a is a tilted-view sketch of the device structure used in the characterization (lower panel) and a corresponding atomic force microscopy image of a typical fabricated device (upper panel). In the device, an InSb nanosheet was contacted by Ti/Au electrodes in a Hall-bar configuration and the carrier density in the nanosheet was modulated by a global back gate. Details about the device parameters can be found in Supporting Information Section S7. First, by voltage-biasing the S and D contacts as shown in Figure 4a, the two-probe conductance G, which takes the form $G = I_{ds}/V_{ds}$, was measured as a function of gate voltage V_{gs} at different temperatures (Figure 4b, main panel, Device 1 with the nanosheet thickness of 50 nm). When lowering temperature, several characteristic features were observed. (1) The off state G shows a monotonic decrease for V_{gs} in the region of −3 to 0 V, while the on state G shows a monotonic increase for V_{gs} in the region of 8 to 10 V. (2) The $G−V_{gs}$ curve becomes steeper in the linear region, indicating an increase of the peak transconductance g_m, where $g_m = \max\{dG/dV_{gs}\}$. (3) A clear ambipolar transport characteristic is seen at $T = 60$ mK with the conductance on the hole side 1−2 orders of magnitude smaller than the electron side (Figure 4b, inset). The observation of the ambipolarity is attributed to the narrow bandgap of InSb and indicates dominant role of hole current in the p-type region at low temperature, while this effect is much less prominent at high temperature, probably masked by thermally activated current of electrons. At this temperature, G can be gate-tuned from $6G_0$ at on state down to $0.008G_0$ at off state ($G_0 = 2e^2/h$, e is the elementary charge, and h is the Planck constant). Moreover, the $G−V_{gs}$ curves are well reproduced for the upward (blue) and downward (red) back-gate-voltage sweep directions, indicating a good surface quality of our InSb nanosheets, free from major influence of interfacial charge traps despite its large surface area. Figure 4c,d shows the $I_{ds}−V_{ds}$ plots at various gate voltages in an n- and a p-type region, respectively. The linear $I_{ds}−V_{ds}$ curves obtained in the n-type region indicate an ohmic behavior in the electron injection and the absence of Schottky contact barrier. On the contrary, the nonlinear $I_{ds}−V_{ds}$ curves observed in the p-type region indicate the presence of injection barrier for holes.

To obtain a reliable field-effect mobility, especially at low temperatures, one needs to take into account the contact

resistance. Here, we adopt a pinch-off trace fitting method.[19,29,41] Yet, a major drawback remains in the approach due to the uncertainty in obtaining the gate-to-nanosheet capacitance C_g. To circumvent it, the Hall-bar device structure was employed to experimentally extract C_g, although C_g could be estimated from the geometric size of the device. Figure 5
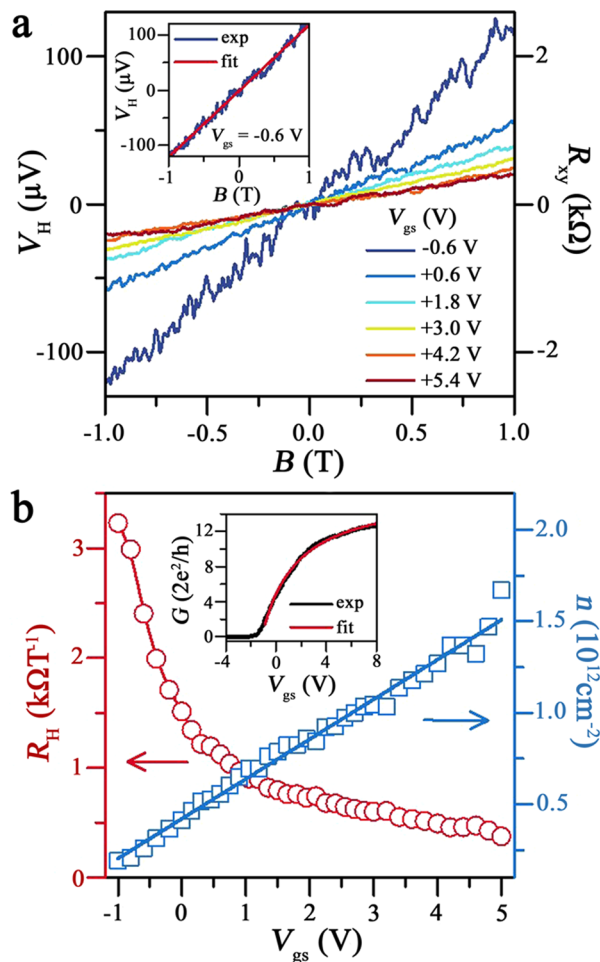

Figure 5. Hall measurements of an InSb nanosheet device. (a) Hall voltage V_H measured as a function of magnetic field B at a constant source-drain current bias of ~50 nA and $T = 60$ mK for several gate voltages (Device 2). The nanosheet thickness of Device 2 is 55 nm. Here, the right axis shows the transverse resistance R_{xy} of the form $R_{xy} = V_H/I$. Note that larger Hall resistance values are found for lower gate voltages (lower carrier densities). The inset shows a linear fit (red) to the measured $V_H−B$ trace (blue) from which the Hall coefficient R_H can be determined. (b) Hall coefficient R_H obtained as a function of V_{gs} (left axis, circle) at $T = 60$ mK. From R_H, we can extract the sheet carrier density n as a function of V_{gs} (right axis, square). A linear fit to the $n−V_{gs}$ data yields $dn/dV_{gs} = 2.1 \times 10^{11}$ cm^{-2} V^{-1} and therefore a gate-to-nanosheet capacitance $C_g = 832$ μF. Using this C_g value, we can fit the measured $G−V_{gs}$ trace of the device (inset panel b) and extract a field-effect mobility of ~15 000 cm^2 V^{-1} s^{-1}.

summarizes the low-field Hall measurement data obtained from a second device (Device 2 with the nanosheet thickness of 55 nm). The Hall resistance, R_{xy}, is gate-tunable and approaches ~2 kΩ at $B \approx 1$ T for the low V_{gs} region (Figure 5a, main panel). A linear fit to the $R_{xy}−B$ curve yields the Hall coefficient (Figure 5a, inset). The carrier density n is then extracted from the gate-dependent Hall coefficient and is found to increase linearly from ~2×10^{11} to ~1.6×10^{12} cm^{-2} with increasing V_{gs}

([Figure 5](#)b, main panel). Then, a gate-to-nanosheet capacitance C_g = 832 μF is determined from the fitting slope of the $n-V_{gs}$ curve, close to the value of ∼800 μF estimated based on the geometry of the device. This measured value is used to fit the two-probe $G-V_{gs}$ curve to evaluate the field-effect mobility of Device 2 ([Figure 5](#)b, inset). The analysis yields an electron mobility of ∼15 000 cm^2 V^{-1} s^{-1} for this device. We have also performed measurements of the Hall mobility for Device 2 at 60 mK using the Hall-bar structure as shown in [Figure 4](#)a. The measurements yielded a Hall mobility of ∼13 000 cm^2 V^{-1} s^{-1} in the high carrier density region, which is close to the field-effect mobility of 15 000 cm^2 V^{-1} s^{-1} obtained with the pinch-off method (see [Supporting Information](#) Section S8 and Figure S15). An electron mobility of ∼18 500 cm^2 V^{-1} s^{-1} is obtained for Device 1 by the same kind of analysis and a hole mobility of ∼90 cm^2 V^{-1} s^{-1} at 60 mK is also obtained from the p-type region of Device 1 (see [Supporting Information](#) Section S8).

In conclusion, we demonstrate a new growth route of high-quality 2D InSb layers by MBE. These InSb layers are free-standing 2D InSb nanosheets grown on 1D InAs nanowires, which is independent of conventional buffer-layer engineering. The morphology and size of InSb nanosheets can be controlled by tailoring the Sb/In BEP ratio and growth time. The length and width of the grown InSb nanosheets can be up to several micrometers and the thickness can be down to ∼10 nm. The InSb nanosheets are pure ZB single crystals. The electrical measurements show that these InSb nanosheets exhibit a high electron mobility and an ambipolar behavior. Our work opens a conceptually new approach to obtaining high-quality 2D narrow bandgap semiconductor nanostructures and will speed up the applications of InSb nanostructures in nanoelectronics, optoelectronics, and quantum electronics and in the development of topological quantum computation technologies.

■ ASSOCIATED CONTENT

ⓢ Supporting Information

The Supporting Information is available free of charge on the [ACS Publications website](#) at DOI: [10.1021/acs.nanolett.5b04845](#).

> Morphology controlling, size and thickness information, detailed crystal structure and quality information, and chemical composition of the InSb nanosheets. Seed-particles information on the InSb nanostructures. A nucleation process of the InSb nanosheets. Summary of the Hall-bar device parameters and extraction of the field-effect mobility and the Hall mobility of a nanosheet. ([PDF](#))

Accession Codes

81.05.Ea; 61.46.Hk; 73.50.Dn; 81.15.Hi

■ AUTHOR INFORMATION

Corresponding Authors

*E-mail: jhzhao@red.semi.ac.cn (J.H.Z.).
*E-mail: hqxu@pku.edu.cn (H.Q.X.).

Notes

The authors declare no competing financial interest.

■ ACKNOWLEDGMENTS

■ REFERENCES

(1) Lundstrom, M. *Science* **2003**, *299*, 210−211.
(2) Chau, R.; Doyle, B.; Datta, S.; Kavalieros, J.; Zhang, K. *Nat. Mater.* **2007**, *6*, 810−812.
(3) Bryllert, T.; Wernersson, L. E.; Froberg, L. E.; Samuelson, L. *IEEE Electron Device Lett.* **2006**, *27*, 323−325.
(4) Ko, H.; Takei, K.; Kapadia, R.; Chuang, S.; Fang, H.; Leu, P. W.; Ganapathi, K.; Plis, E.; Kim, H. S.; Chen, S. Y.; Madsen, M.; Ford, A. C.; Chueh, Y. L.; Krishna, S.; Salahuddin, S.; Javey, A. *Nature* **2010**, *468*, 286−289.
(5) Tomioka, K.; Yoshimura, M.; Fukui, T. *Nature* **2012**, *488*, 189−193.
(6) Wolf, S. A.; Awschalom, D. D.; Buhrman, R. A.; Daughton, J. M.; von Molnár, S.; Roukes, M. L.; Chtchelkanova, A. Y.; Tresger, D. M. *Science* **2001**, *294*, 1488−1495.
(7) Zutic, I.; Das Sarma, S. *Rev. Mod. Phys.* **2004**, *76*, 323−410.
(8) Sau, J. D.; Tewari, S.; Das Sarma, S. *Phys. Rev. Lett.* **2010**, *104*, 040502−040505.
(9) Alicea, J. *Phys. Rev. B: Condens. Matter Mater. Phys.* **2010**, *81*, 125318−125327.
(10) Mourik, V.; Zuo, K.; Frolov, S. M.; Plissard, S. R.; Bakkers, E. P. A. M.; Kouwenhoven, L. P. *Science* **2012**, *336*, 1003−1007.
(11) Deng, M. T.; Yu, C. L.; Huang, G. Y.; Larsson, M.; Caroff, P.; Xu, H. Q. *Nano Lett.* **2012**, *12*, 6414−6419.
(12) Deng, M. T.; Yu, C. L.; Huang, G. Y.; Larsson, M.; Caroff, P.; Xu, H. Q. *Sci. Rep.* **2014**, *4*, 7261−7268.
(13) Rokhinson, L. P.; Liu, X. Y.; Furdyna, J. K. *Nat. Phys.* **2012**, *8*, 795−799.
(14) Vurgaftman, I.; Meyer, J. R.; Ram-Mohan, L. R. *J. Appl. Phys.* **2001**, *89*, 5815−5875.
(15) Nilsson, H. A.; Caroff, P.; Thelander, C.; Larsson, M.; Wagner, J. B.; Wernersson, L. E.; Samuelson, L.; Xu, H. Q. *Nano Lett.* **2009**, *9*, 3151−3156.
(16) Nilsson, H. A.; Karlström, O.; Larsson, M.; Caroff, P.; Pedersen, J. N.; Samuelson, L.; Wacker, A.; Wernersson, L. E.; Xu, H. Q. *Phys. Rev. Lett.* **2010**, *104*, 186804−186807.
(17) Nilsson, H. A.; Samuelsson, P.; Caroff, P.; Xu, H. Q. *Nano Lett.* **2012**, *12*, 228−233.
(18) Fan, D.; Li, S.; Kang, N.; Caroff, P.; Wang, L. B.; Huang, Y. Q.; Deng, M. T.; Yu, C. L.; Xu, H. Q. *Nanoscale* **2015**, *7*, 14822−14828.
(19) Plissard, S. R.; van Weperen, I.; Car, D.; Verheijen, M. A.; Immink, G. W. G.; Kammhuber, I. J.; Cornelissen, L. J.; Szombati, D. B.; Geresdi, A.; Frolov, S. M.; Kouwenhoven, L. P.; Bakkers, E. P. A. M. *Nat. Nanotechnol.* **2013**, *8*, 859−864.
(20) Car, D.; Wang, J.; Verheijen, M. A.; Bakkers, E. P. A. M.; Plissard, S. R. *Adv. Mater.* **2014**, *26*, 4875−4879.
(21) Weng, X.; Rudawski, N. G.; Wang, P. T.; Goldman, R. S.; Partin, D. L.; Heremans, J. *J. Appl. Phys.* **2005**, *97*, 043713−043719.
(22) Mishima, T. D.; Edirisooriya, M.; Goel, N.; Santos, M. B. *Appl. Phys. Lett.* **2006**, *88*, 191908−191910.
(23) Pan, D.; Fu, M. Q.; Yu, X. Z.; Wang, X. L.; Zhu, L. J.; Nie, S. H.; Wang, S. L.; Chen, Q.; Xiong, P.; von Molnár, S.; Zhao, J. H. *Nano Lett.* **2014**, *14*, 1214−1220.
(24) Vogel, A. T.; de Boor, J.; Becker, M.; Wittemann, J. V.; Mensah, S. L.; Werner, P.; Schmid, V. *Nanotechnology* **2011**, *22*, 015605−015610.
(25) Mandl, B.; Dick, K. A.; Kriegner, D.; Keplinger, M.; Bauer, G.; Stangl, J.; Deppert, K. *Nanotechnology* **2011**, *22*, 145603−145609.
(26) Lin, A.; Shapiro, J. N.; Eisele, H.; Huffaker, D. L. *Adv. Funct. Mater.* **2014**, *24*, 4311−4316.
(27) Caroff, P.; Wagner, J. B.; Dick, K. A.; Nilsson, H. A.; Jeppsson, M.; Deppert, K.; Samuelson, L.; Wallenberg, R.; Wernersson, L. E. *Small* **2008**, *4*, 878−882.

(28) Ercolani, D.; Rossi, F.; Li, A.; Roddaro, S.; Grillo, V.; Salviati, G.; Beltram, F.; Sorba, L. *Nanotechnology* **2009**, *20*, 505605−505610.

(29) Plissard, S. R.; Slapak, D. R.; Verheijen, M. A.; Hocevar, M.; Immink, G. W. G.; van Weperen, I.; Nadj-Perge, S.; Frolov, S. M.; Kouwenhoven, L. P.; Bakkers, E. P. A. M. *Nano Lett.* **2012**, *12*, 1794−1798.

(30) Thelander, C.; Caroff, P.; Plissard, S.; Dick, K. A. *Appl. Phys. Lett.* **2012**, *100*, 232105−232108.

(31) de la Mata, M.; Magen, C.; Caroff, P.; Arbiol, J. *Nano Lett.* **2014**, *14*, 6614−6620.

(32) Wagner, R. S.; Ellis, W. C. *Appl. Phys. Lett.* **1964**, *4*, 89−90.

(33) Morales, A. M.; Lieber, C. M. *Science* **1998**, *279*, 208−211.

(34) Pan, Z. W.; Dai, Z. R.; Wang, Z. L. *Science* **2001**, *291*, 1947−1949.

(35) Lugani, L.; Ercolani, D.; Rossi, F.; Salviati, G.; Beltram, F.; Sorba, L. *Cryst. Growth Des.* **2010**, *10*, 4038−4042.

(36) Lugani, L.; Ercolani, D.; Beltram, F.; Sorba, L. *J. Cryst. Growth* **2011**, *323*, 304−306.

(37) Li, A.; Sibirev, N. V.; Ercolani, D.; Dubrovskii, V. G.; Sorba, L. *Cryst. Growth Des.* **2013**, *13*, 878−882.

(38) Plissard, S.; Dick, K. A.; Wallart, X.; Caroff, P. *Appl. Phys. Lett.* **2010**, *96*, 121901−121903.

(39) Nimmatoori, P.; Zhang, Q.; Dickey, E. C.; Redwing, J. M. *Nanotechnology* **2009**, *20*, 025607−025612.

(40) de la Mata, M.; Leturcq, R.; Plissard, S. R.; Rolland, C.; Magen, C.; Arbiol, J.; Caroff, P. *Nano Lett.* **2016**, DOI: 10.1021/acs.nanolett.5b05125.

(41) Gül, Ö.; van Woerkom, D. J.; van Weperen, I.; Car, D.; Plissard, S. R.; Bakkers, E. P. A. M.; Kouwenhoven, L. P. *Nanotechnology* **2015**, *26*, 215202−215208.